## EDGE ARTICLE

Check for updates

All publication charges for this article have been paid for by the Royal Society of Chemistry

# Leveraging phenazine and dihydrophenazine redox dynamics in conjugated microporous polymers for high-efficiency overall photosynthesis of hydrogen peroxide†

Shufan Feng‡[a] Lei Wang‡[b] Limei Tian‡[c] Ying Liu‡[d] Ke Hu, [iD][c] Hangxun Xu, [iD]*[b] Haifeng Wang [iD]*[d] and Jianli Hua [iD]*[a]

Harnessing solar energy for hydrogen peroxide ($H_2O_2$) production from water and oxygen is crucial for sustainable solar fuel generation. Conjugated microporous polymers (CMPs), with their vast structural versatility and extended π-conjugation, are promising photocatalysts for solar-driven $H_2O_2$ generation, though enhancing their efficiency is challenging. Inspired by the crucial role of phenazine derives in biological redox cycling and electron transfer processes, the redox-active phenazine moiety is rationally integrated into a CMP framework (TPE-PNZ). By leveraging the reversible redox dynamics between phenazine and dihydrophenazine, TPE-PNZ sets a new benchmark for $H_2O_2$ production among CMP-based photocatalysts, reaching a production rate of 5142 $\mu$mol g$^{-1}$ h$^{-1}$ and a solar-to-chemical conversion efficiency of 0.58% without requiring sacrificial agents. This interconversion allows for the storage of photogenerated electrons by phenazine and subsequent conversion into dihydrophenazine, which then reduces $O_2$ to $H_2O_2$ while reverting to phenazine, markedly facilitating charge transfer and mitigating charge recombination. Experimental and computational investigations further reveal that this reversible process enhances $O_2$ adsorption and reduction, significantly lowering the energy barrier towards $H_2O_2$ formation. This study offers critical insights into designing advanced materials for sustainable energy research.

## Introduction

The escalating global demand for hydrogen peroxide ($H_2O_2$), anticipated to reach 5.7 million tons by 2027, demonstrates its indispensable role across various application areas, including papermaking, mining, chemical engineering, and water treatment.[1] The conventional reliance on the anthraquinone process for industrial $H_2O_2$ production, despite its high efficacy, raises significant environmental and energy consumption concerns, given its high energy inputs and hazardous waste outputs.[2] These challenges have spurred the search for alternative green and sustainable production methodologies, with artificial photosynthesis at the forefront as a viable and promising solution.[3] Nevertheless, this technology is still far from commercial viability for scalable $H_2O_2$ production. The primary impediment stems from the fact that the efficiency and stability of current photocatalysts fail to meet the stringent demands of industrial applications. This discrepancy highlights the urgent necessity for the innovative creation of photocatalysts that are not only cost-efficient and robust but also exhibit superior efficiency.[4]

Conjugated microporous polymers (CMPs) emerge as a novel class of polymer photocatalysts for solar-driven $H_2O_2$ production, owing to their extensive π-electron systems, high surface areas, and flexibility in their structural modification. However, despite these fascinating characteristics, the photocatalytic efficiency of CMPs is often compromised by pronounced charge recombination and high energy barriers during $H_2O_2$ generation.[5] To address these limitations, research has ventured into incorporating diverse functional groups into CMPs, such as triazines, thiophenes, and furans, aiming to enhance

photocatalytic performances of CMPs.[6] Unfortunately, CMP-based photocatalysts still tend to underperform when compared to other polymer photocatalysts such as resorcinol–formaldehyde resins, covalent organic frameworks, and g-$C_3N_4$ derivatives.[7] Thus, enhancing the photocatalytic efficiency of CMPs through molecular engineering, particularly by introducing innovative redox-active groups that can improve charge transfer and lower the energy threshold for $H_2O_2$ production, is highly desirable.[8]

Phenazines are naturally abundant compounds that can be synthesized by various bacteria, including strains of *Pseudomonas* and *Streptomyces*.[9] These compounds can undergo redox cycling within biological systems, oscillating between oxidized (phenazine) and reduced (dihydrophenazine) states. The interconversion between phenazine and dihydrophenazine has essential implications in biological systems, including redox reactions, electron transfer, and cellular signaling.[10] In light of the exceptional ability of phenazine-based compounds to transfer electrons and their pivotal role in redox reactions within biological systems, integrating phenazine as a functional group into the structure of CMPs could potentially enhance their performances in photocatalytic $H_2O_2$ production. This makes phenazine an excellent candidate for designing CMPs with enhanced photocatalytic efficiency.

In this study, we show that the unique redox-active property of phenazine can be leveraged to develop a phenazine-incorporated CMP (TPE-PNZ) to enhance the photocatalytic production of $H_2O_2$ from $H_2O$ and $O_2$. The integration of phenazine into TPE-PNZ allows it to serve as an effective electron transfer mediator, reflecting its role in natural microbial redox processes. This capability enables the transition of phenazine to dihydrophenazine through the photoreduction process, facilitating the reduction of $O_2$ to $H_2O_2$, while dihydrophenazine can be oxidized by oxygen to regenerate phenazine. As a result, TPE-PNZ achieves an impressive $H_2O_2$ production rate of 5142 $\mu$mol g$^{-1}$ h$^{-1}$ and a remarkable solar-to-chemical conversion (SCC) efficiency of 0.58%. This is in stark contrast to a similarly designed CMP without the phenazine component, TPE-AC, which exhibits a much reduced $H_2O_2$ production rate, highlighting the critical role of the reversible phenazine/dihydrophenazine conversion in enhancing photocatalytic efficiency. Further studies indicate that the strategically incorporated phenazine enhances both the adsorption and reduction of $O_2$, effectively lowering the energy barrier for $H_2O_2$ production. This study not only introduces a valuable functional moiety for the design of CMPs but also offers substantial insights into optimizing charge dynamics and active sites within CMPs for future solar fuel production.

## Results and discussion

As shown in Fig. 1a, TPE-PNZ and TPE-AC were synthesized *via* Sonogashira coupling reactions using tetrakis(4-ethynylphenyl) ethane (TEPE) with 2,7-dibromophenazine (PNZ-Br) and 2,6-dibromoanthracene (AC-Br), respectively. The detailed synthetic routes are illustrated in Fig. S1 and S2.† In this manner, the phenazine unit was rationally integrated into TPE-PNZ, creating a donor–acceptor (D–A) structure through the interaction of the electron-deficient phenazine and the electron-rich TEPE. The Fourier transform infrared (FTIR) spectra, shown in Fig. 1b, were employed to confirm the chemical structures of TPE-PNZ and TPE-AC. The stretching vibration peaks around 3275 cm$^{-1}$ can be attributed to the $\equiv$C–H bonds of the terminal alkynes in TEPE, while the peaks at 1042 cm$^{-1}$ in PNZ-Br and AC-Br correspond to the C–Br bond. Remarkably, the characteristic stretching vibration peaks observed in the precursors are absent in the spectra of TPE-PNZ and TPE-AC, suggesting the complete polymerization of TEPE with PNZ-Br and AC-Br, respectively.[11] In addition, the high-resolution C 1s X-ray photoelectron spectroscopy (XPS) spectra of TPE-PNZ display peaks at approximately 282.0, 284.0, and 286.0 eV (Fig. 1c), which can be assigned to the C=C, C$\equiv$C, and C=N bond, respectively.[12] In contrast, the peak associated with the C=N bond cannot be found in the XPS spectra of TPE-AC. The chemical structures of both CMPs were further characterized by solid-state $^{13}$C NMR spectroscopy (Fig. 1d). For TPE-PNZ, peaks in the range of 120–140 ppm are ascribed to aromatic carbons, and peaks at 90 ppm are associated with carbon atoms in the alkyne groups. Moreover, the peaks at 170 ppm can be attributed to the carbon atoms in phenazine moieties, which are not observed from the spectrum of TPE-AC.[13] These characterizations conclusively confirmed the successful synthesis of designed CMPs.

The powder X-ray diffraction (PXRD) patterns, as shown in Fig. S3,† reveal that both TPE-PNZ and TPE-AC polymers possess amorphous structures. Both TPE-PNZ and TPE-AC exhibit irregularly aggregated particle structures as observed from scanning electron microscopy (SEM) and transmission electron microscopy (TEM) images (Fig. S4 and S5†). This observation is consistent for both TPE-PNZ and TPE-AC, highlighting a common structural feature despite they incorporate different functional moieties. Meanwhile, energy-dispersive X-ray spectroscopy (EDS) mapping confirms the homogeneous distribution of carbon (C) and nitrogen (N) elements across the surface of TPE-PNZ (Fig. S6†). The uniform distribution of elements further suggests that the phenazine moieties are well-integrated throughout the polymer framework.[14] The $N_2$ sorption measurements were conducted at 77 K to assess the permanent porosity of both CMPs (Fig. S7†). The measured Brunauer–Emmett–Teller (BET) surface areas of TPE-PNZ and TPE-AC are 722.4 and 759.6 m$^2$ g$^{-1}$, respectively. Notably, the primary pore sizes were found to be below 2 nm, indicating predominantly microporous structures for both TPE-PNZ and TPE-AC. The microporosity of TPE-PNZ and TPE-AC can be particularly advantageous for photocatalytic applications, providing abundant active sites for photocatalytic reactions and facilitating efficient mass transfer.[15] Furthermore, it is noteworthy that the $N_2$ adsorption/desorption isotherms of TPE-PNZ and TPE-AC do not exhibit closure. The phenomenon may result from a variety of reasons related to the physical and chemical environments experienced by $N_2$ molecules during the adsorption/desorption process. During adsorption, $N_2$ molecules can penetrate deeply into the micropores, causing the pores to swell and the polymer structure to reorganize. This
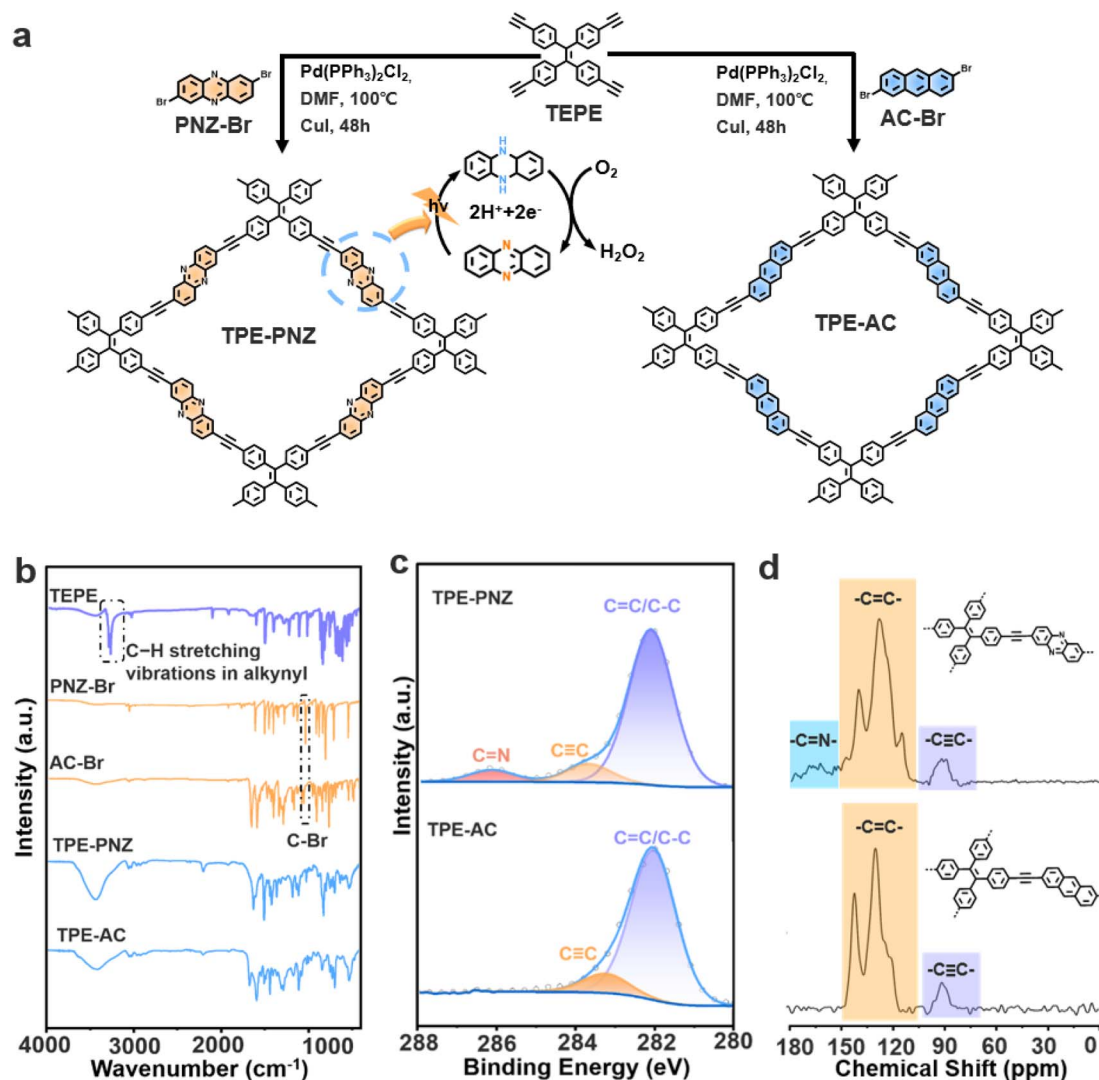
Fig. 1 (a) Schematic illustration of the synthetic routes towards TPE-PNZ and TPE-AC from their corresponding precursors. (b) FTIR spectra of TPE-PNZ, TPE-AC, and their corresponding precursors. (c) High-resolution C 1s XPS spectra of TPE-PNZ and TPE-AC. (d) Solid-state $^{13}$C NMR spectra of TPE-PNZ and TPE-AC.

reorganization can create new pathways and barriers that alter the adsorption dynamics. During desorption, $N_2$ molecules encounter different kinetic barriers compared to adsorption. These barriers can include narrow pore openings, irregular pore shapes, and variations in pore connectivity, which can slow down or hinder the release of $N_2$ molecules. The process of adsorption and desorption may follow different thermodynamic pathways. This can result in the isotherms not overlapping perfectly, especially at lower pressures where the effects of pore structure and molecular interactions are more pronounced.[16,17]

Fig. 2a presents the UV-vis diffuse reflectance spectroscopy spectra of both CMPs, which exhibit pronounced absorption within the visible light range, indicating their potential for solar-driven photocatalytic applications. Based on the Tauc plots, the optical bandgaps were determined to be approximately 2.19 eV for TPE-PNZ and 2.01 eV for TPE-AC (Fig. S8†).[18]

Meanwhile, the positive slope observed in the Mott–Schottky plots for the CMPs implied that both CMPs were n-type semiconductors (Fig. S9†). This characteristic is crucial for their photocatalytic applications, indicating efficient electron conduction upon photoexcitation.[19] The flat band potentials of TPE-PNZ and TPE-AC, when measured against the saturated calomel electrode (SCE) at a neutral pH of 7, were identified to be −0.63 and −0.56 V, respectively. Consequently, the conduction band (CB) levels were calculated to be −0.59 V for TPE-PNZ and −0.52 V for TPE-AC relative to the normal hydrogen electrode (NHE).[20] Therefore, the band structures of both TPE-PNZ and TPE-AC are well-positioned for photocatalytic $H_2O_2$ production from pure water without using any sacrificial agents (Fig. 2b).[3]

The photocatalytic performances of TPE-PNZ and TPE-AC were assessed in pure water under visible-light irradiation ($\lambda >$ 420 nm). As shown in Fig. 2c, TPE-PNZ demonstrates
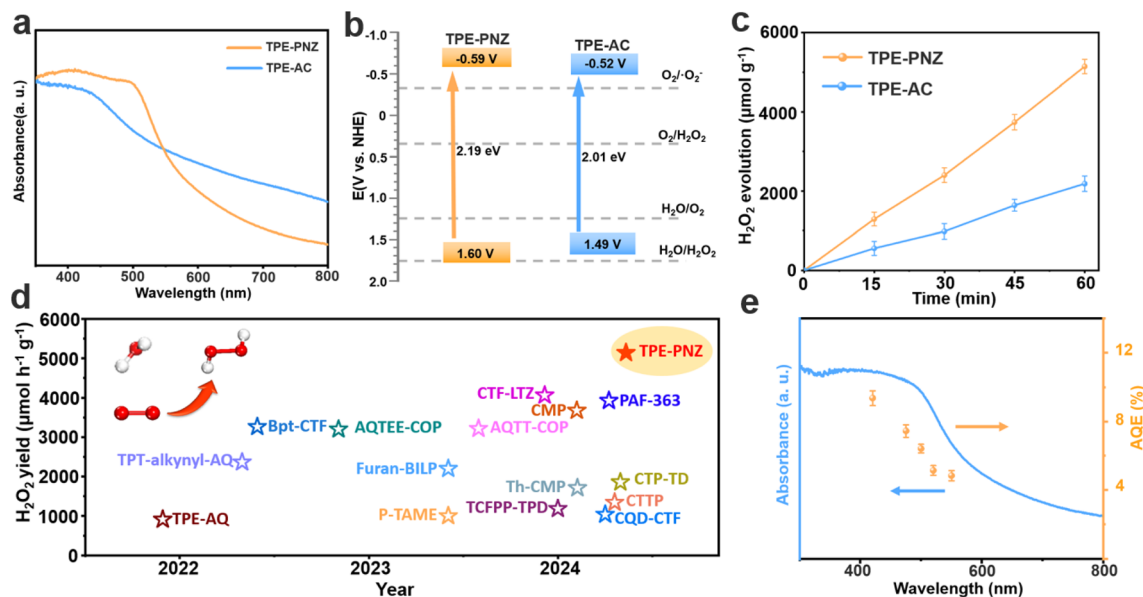
Fig. 2 (a) UV/vis DRS spectra and (b) band structures of TPE–PNZ and TPE–AC. (c) Typical time course of $H_2O_2$ production in pure water using TPE–PNZ and TPE–AC, error bars are derived from standard errors from three tests. (d) Summary of $H_2O_2$ production rates from recently reported CMP-based photocatalysts for $H_2O_2$ production. (e) Wavelength-dependent AQEs of TPE–PNZ, error bars are derived from standard errors from three tests.

a remarkable $H_2O_2$ production rate of 5142 μmol g$^{-1}$ h$^{-1}$, surpassing all previously reported CMP-based photocatalysts (Fig. 2d).[5,11,21–34] Meanwhile, TPE–PNZ achieved an impressive SCC efficiency of 0.58%, surpassing most CMP-based photocatalysts reported to date (Table S1†). In contrast, TPE–AC, designed as a comparative benchmark by replacing phenothiazine with anthracene in TPE–PNZ, only exhibited a much lower $H_2O_2$ production rate of 2183 μmol g$^{-1}$ h$^{-1}$. This observation indicates that the phenazine moiety plays a crucial role in enhancing the photocatalytic activity towards $H_2O_2$ generation. The apparent quantum efficiency (AQE) of TPE–PNZ at a wavelength of 420 nm was calculated to be 9.37%. The AQE values across different wavelengths correlate well with the absorption spectrum of TPE–PNZ, as illustrated in Fig. 2e. Notably, TPE–PNZ also exhibits a high photocatalytic $H_2O_2$ production rate in seawater (5250 μmol g$^{-1}$ h$^{-1}$), indicating that its photocatalytic activity would not be influenced by the high concentration of ions in seawater (Fig. S10†). This observation indicates that the as-synthesized TPE–PNZ holds great potential for solar-driven $H_2O_2$ production from seawater.[35]

The stability of TPE–PNZ, an essential aspect of performance evaluation, was confirmed through cyclic tests showing that TPE–PNZ retains its prominent $H_2O_2$ production rate after five rounds of photoirradiation (Fig. S11†). In addition, FTIR and XPS measurements revealed no substantial changes in the chemical structure of TPE–PNZ, evidencing that CMPs with fully π conjugated structures are highly robust photocatalysts for the photosynthesis of $H_2O_2$ (Fig. S12†). Both TPE–PNZ and TPE–AC exhibited minimal $H_2O_2$ decomposition activity, suggesting that the variance in $H_2O_2$ production rates between them is not due to their $H_2O_2$ decomposition capabilities (Fig. S13†).[3] Furthermore, inductively coupled plasma (ICP) analyses found

no obvious correlation between the photocatalytic performances of TPE–PNZ and TPE–AC and their residual Pd contents (Table S2†). This finding rules out the possibility that the performance difference between the two CMPs is caused by different Pd content levels.[36]

In biological systems, phenazine derivatives are produced by certain microorganisms and play a crucial role in electron transfer processes.[9] TPE–PNZ exhibits notably enhanced photocatalytic performance compared to TEP–AC, implying that the redox-active phenazine moiety has a significant impact on the charge transfer process in CMPs. The comparative analysis of photocurrent responses and electrochemical impedance spectroscopy (EIS) measurements for TPE–PNZ and TPE–AC are presented in Fig. 3a and b, respectively. Here, TPE–PNZ demonstrates a substantially enhanced photocurrent with lower electrochemical impedance, implying that the phenazine moiety can facilitate charge separation.[37] Additionally, we also evaluated the internal electric fields within CMPs by measuring their surface voltages and surface charge densities (Fig. 3c and S14†). The results reveal that TPE–PNZ exhibits an enhanced built-in electric field intensity (3.94) compared to TPE–AC (1.00), providing further evidence that the phenazine component can effectively promote charge separation.[38] Density functional theory (DFT) calculations were then utilized to elucidate the differences in charge transfer dynamics between TPE–PNZ and TPE–AC (Fig. 3d). For TPE–PNZ, photoexcitation prompts a transition from the highest occupied molecular orbital (HOMO) to the lowest unoccupied molecular orbital (LUMO), resulting in an electron density shift from the TPE segments to the phenazine units. This redistribution facilitates effective intramolecular charge transfer within the π-conjugated framework. In contrast, for TPE–AC, DFT calculations show that both
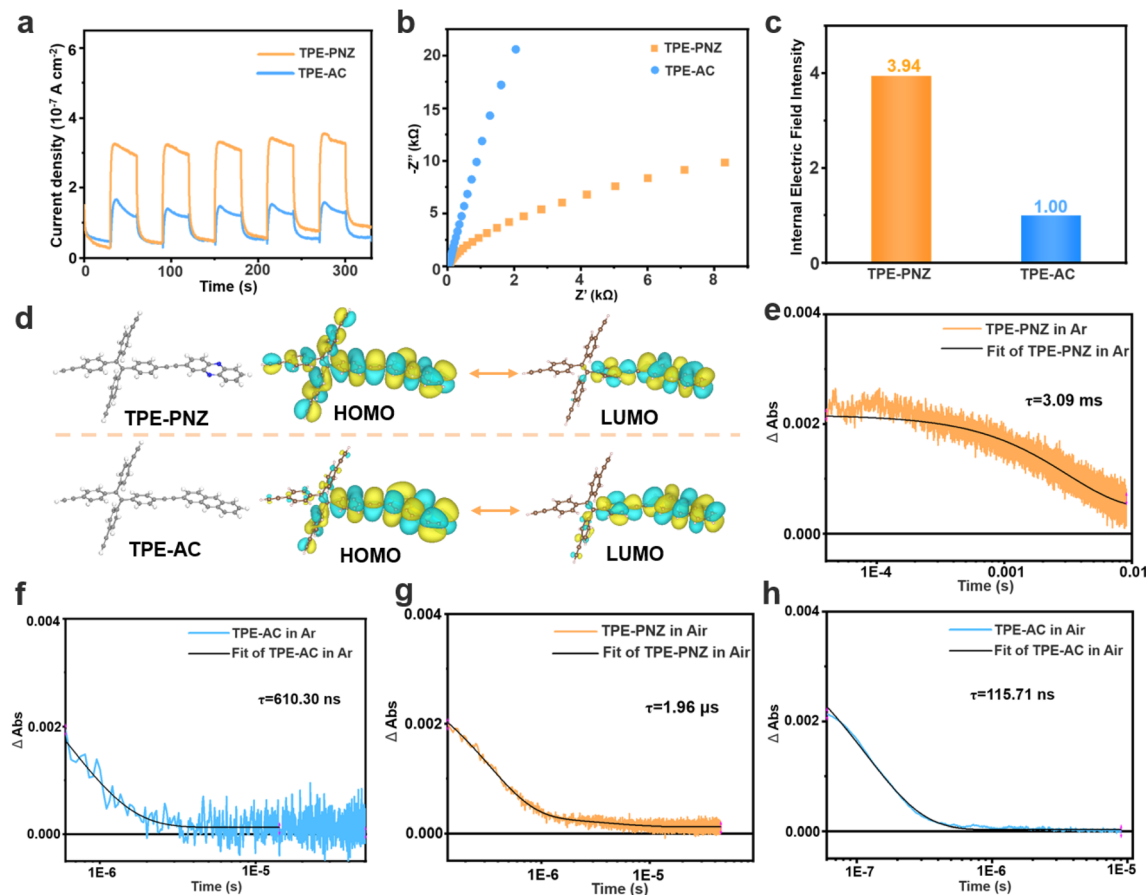
Fig. 3 (a) Transient photocurrents, (b) Nyquist plots, and (c) relative internal electric field intensities of TPE–PNZ and TPE–AC. (d) The calculated distribution of the HOMO and LUMO of TPE–PNZ and TPE–AC. The TA kinetics trace of (e) TPE–PNZ and (f) TPE-AC probed at 500 nm under Ar. The TA kinetics trace of (g) TPE–PNZ and (h) TPE-AC probed at 500 nm under air.

HOMO and LUMO levels are uniformly distributed throughout the entire polymer framework. The uniform distribution of HOMO and LUMO levels is unfavorable for charge separation within the polymer framework due to the lack of a preferential direction or region for the dynamic movement of photo-generated electrons and holes.[39] We also utilized nanosecond transient absorption (ns-TA) spectroscopy to probe the dynamics of photogenerated charge carriers within CMPs. Based on the results of the spectroelectrochemical test (Fig. S15†), the absorption peak at 500 nm in the TA spectra of both TPE-PNZ and TPE-AC corresponds to their photoinduced charge-separated states.[40] As shown in Fig. 3e and f, the average relaxation lifetime of photoinduced charge-separated states in TPE-PNZ under an Ar atmosphere is 3.09 ms, which is about 5060 times the lifetime observed for TPE-AC (610.30 ns). This stark contrast substantiates the vital role of the phenazine moiety in enhancing charge transfer efficiency and inhibiting charge recombination.[12] Under an ambient air environment, the charge separation lifetimes for TPE-PNZ and TPE-AC decrease markedly to 1.96 μs and 115.71 ns, respectively (Fig. 3g and h). Our calculations reveal that the quenching effect of $O_2$ on the charge separation lifetime of TPE-PNZ reaches an efficiency of 99.98%, notably higher than that for TPE-AC, which

is only 81.01%. This demonstrates a faster electron transfer from TPE-PNZ to $O_2$ as compared to TPE-AC, highlighting the significance of phenazine moiety in enhancing the interaction with $O_2$ and improving the efficiency of $O_2$ reduction to $H_2O_2$.[41]

A series of control experiments were conducted to elucidate the mechanism responsible for photocatalytic $H_2O_2$ production. Fig. S16† demonstrates that no $H_2O_2$ production was observed under the $N_2$ atmosphere, confirming that $H_2O_2$ is generated through the reduction of $O_2$. We also performed steady-state fluorescence tests on TPE-PNZ and TPE-AC under Ar and $O_2$ conditions, respectively. The experimental results showed that the fluorescence of both catalysts could be quenched by $O_2$, confirming the efficient transfer of photo-generated electrons to $O_2$ for the production of $H_2O_2$ (Fig. S17†).[42,43] To further unravel reactive species during $H_2O_2$ formation, radical trapping experiments were carried out. These experiments revealed that the introduction of AgNO$_3$ led to the absence of $H_2O_2$ detection while adding 10% benzyl alcohol notably enhanced $H_2O_2$ production, reflecting that $H_2O_2$ synthesis in both CMPs is a result of the $O_2$ reduction process.[44] The introduction of *para*-benzoquinone (*p*-BQ) into the reaction system inhibited $H_2O_2$ production, further suggesting that superoxide radicals (˙$O_2^-$) act as the primary intermediates in

$H_2O_2$ formation, through a mechanism involving stepwise single-electron transfer process ($O_2 \rightarrow \,^{\cdot}O_2^- \rightarrow H_2O_2$).[45] This mechanism is corroborated by the results obtained from electron paramagnetic resonance (EPR) spectroscopic measurements, with the EPR spectra of TPE-PNZ under visible light showing distinctive peaks for the DMPO-$^{\cdot}O_2^-$ adducts (Fig. S18a†). On the other hand, the absence of DMPO-$^{\cdot}$OH spin adduct peaks in the EPR spectra of TPE-PNZ when AgNO$_3$ was employed as an electron scavenger under light irradiation (Fig. S18b†) rules out the possibility of hydroxyl radicals ($^{\cdot}$OH) formation through water oxidation. Moreover, only O$_2$ can be detected when AgNO$_3$ is used as an electron scavenger, implying that photogenerated holes in TPE-PNZ oxidize water to produce O$_2$ through a four-electron process (Fig. S19†).[46] The average electron transfer number for the O$_2$ reduction reactions, as determined from the RDE tests, is calculated to be 2.05 and 1.66 for TPE-PNZ and TPE-AC, respectively (Fig. S20†). This indicates that the incorporation of the phenazine moiety into the CMP framework is beneficial for the conversion of O$_2$ into H$_2$O$_2$ via the two-electron reduction pathway.[14,45] We also monitored the changes in the photocatalytic system's pH value over time. As shown in Fig. S21,† no detectable change in the pH value of the solution can be observed over time.[47,48]

*In situ* diffuse reflectance infrared Fourier transform spectroscopy (DRIFTS) measurements were carried out to further explore the mechanism for H$_2$O$_2$ production from TPE-PNZ. As illustrated in Fig. 4a, spectral features appearing at 1384 and 1260 cm$^{-1}$ can be attributed to the stretching vibrations of C–N

and C=N bonds in TPE-PNZ, respectively.[49,50] Upon exposure to visible light under the Ar atmosphere, there was a noticeable decrease in the intensity of the C=N bond peak within the phenazine units, along with an increase in the C–N bond peak intensity. This observation provides strong evidence that the phenazine moiety in TPE-PNZ can be photochemically reduced to dihydrophenazine under photoirradiation. To better illustrate the conversion process from phenazine to dihydrophenazine, we overlaid the curves in the spectrum (Fig. S22†). It's note that in spectroscopic analyses, changes in peak intensity are more pronounced during the initial stages of the reaction. This phenomenon can be attributed to the system approaching equilibrium between the interconversion of phenazine and dihydrophenazine under the given reaction conditions. Once equilibrium is established, the rate at which peak intensities change diminishes, reflecting the characteristic behavior of dynamic equilibrium systems where the rates of forward and reverse reactions balance over time.[23,51–53] Meanwhile, the continuous production of H$_2$O$_2$, even in the absence of light, further indicates that the phenazine moiety is capable of storing electrons (Fig. S23†).[54] In contrast, when O$_2$ was purged under dark conditions, the peak intensity of the C–N bond gradually decreased, whereas the intensity of the peak corresponding to the C=N band gradually increased (Fig. 4b), suggesting that O$_2$ can oxidize dihydrophenazine back to phenazine. Notably, no significant changes in the intensities of C–N and C=N bands were observed when TPE-PNZ was irradiated under light with O$_2$ purging, as shown in Fig. 4c. This
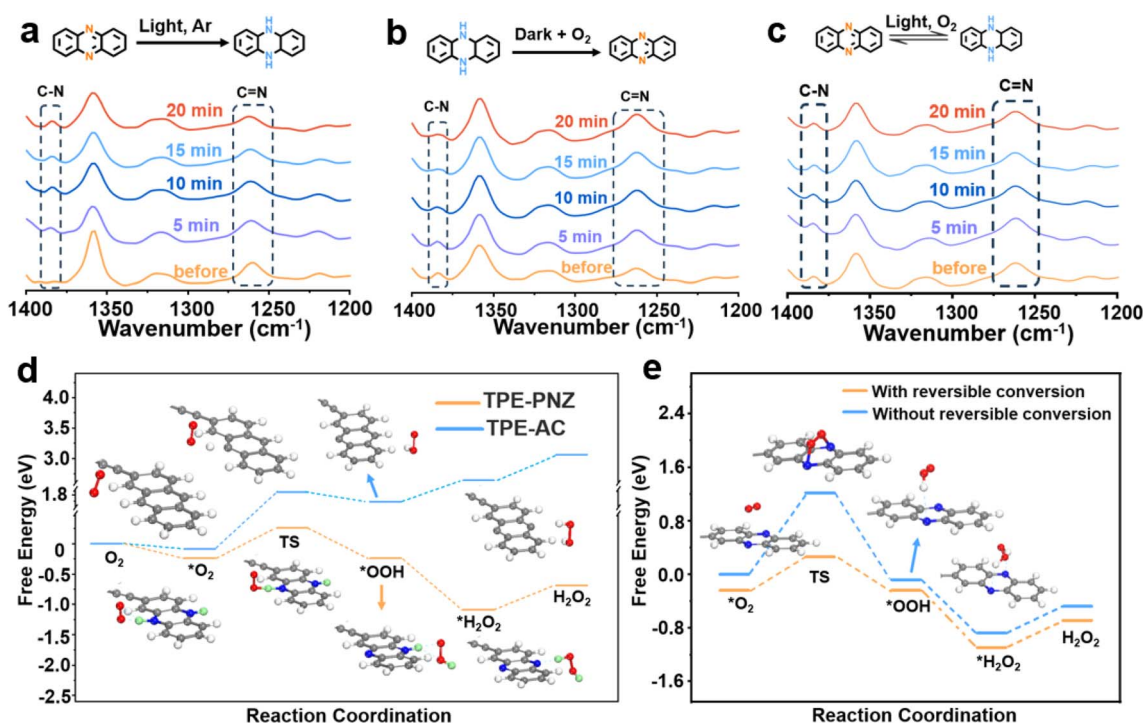


Fig. 4 (a) *In situ* DRIFT spectra of TPE–PNZ saturated with Ar under visible light irradiation. (b) *In situ* DRIFT spectra of TPE–PNZ saturated with O$_2$ under dark. (c) *In situ* DRIFT spectra of TPE–PNZ saturated with O$_2$ under visible light irradiation. (d) Free energy diagrams of TPE–PNZ and TPE–AC for the photosynthesis of H$_2$O$_2$ via the oxygen reduction process. (e) Comparison of the Gibbs free energy for H$_2$O$_2$ production with and without the interconversion of phenazine and dihydrophenazine in TPE–PNZ.
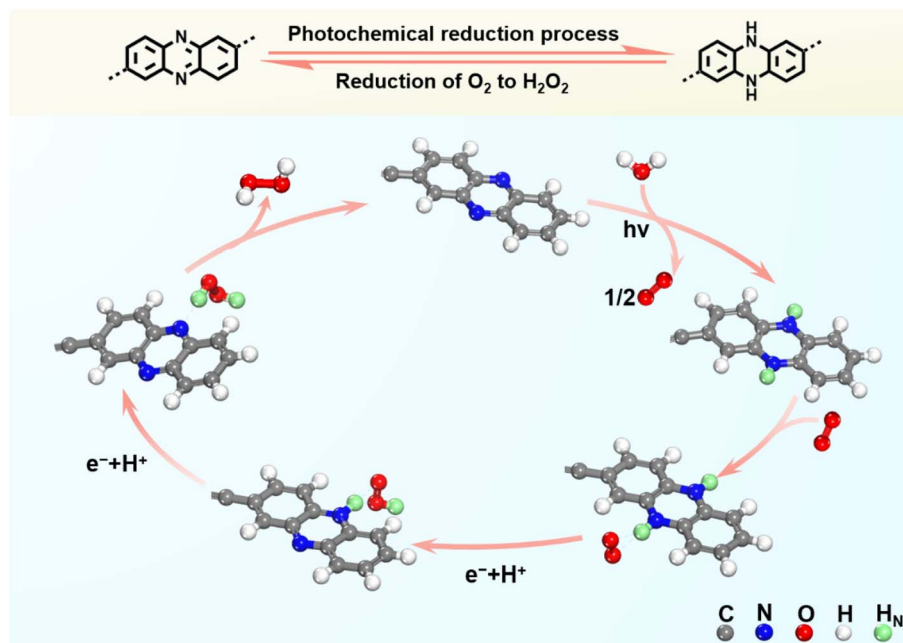
**Fig. 5** Schematic illustration of the reversible transformation between phenazine and dihydrophenazine in TPE-PNZ during $H_2O_2$ production. (Color denotation: gray: C; blue: N; red: O; white: H in benzene; green: H in dihydrophenazine).

suggests the existence of a dynamic equilibrium between phenazine and dihydrophenazine in the presence of $O_2$ under photoirradiation. Additionally, it suggests that during the photocatalytic production of $H_2O_2$, the rate of water oxidation matches the rate of $O_2$ reduction.[25,51,52] The insights from the *in situ* DRIFTS measurements conclusively demonstrate the reversible interconversion between phenazine and dihydrophenazine during the photocatalytic generation of $H_2O_2$ by TPE-PNZ.[51]

DFT calculations were performed to thoroughly understand how the rationally embedded phenazine moiety in TPE-PNZ can facilitate $H_2O_2$ production. These calculations pinpointed the rate-determining step of the stepwise single-electron $O_2$ reduction reaction in both TPE-PNZ and TPE-AC as the formation of the *OOH intermediate.[45] For TPE-PNZ, electrons generated upon photoexcitation initially reduce phenazine to dihydrophenazine (Fig. 4d). This is followed by the adsorption of $O_2$ onto dihydrophenazine, where it gains an electron and a proton to form *OOH. For TPE-AC, anthracene acts as the adsorption site for both $*O_2$ and *OOH. The Gibbs free energy for *OOH formation on TPE-AC (1.69 eV) is much higher than that on TPE-PNZ (−0.24 eV). This disparity indicates that the phenazine moiety can drastically lower the energy requirement for *OOH formation, thereby enhancing the efficiency of $H_2O_2$ production.[1] To further validate the impact of the reversible interconversion between phenazine and dihydrophenazine on $H_2O_2$ generation, we also simulated the photocatalytic pathways for $H_2O_2$ production in TPE-PNZ by excluding the reversible interconversion process. In this model, $*O_2$ is protonated by the surrounding medium to yield *OOH,[14] with the *OOH adsorption occurring at the N atom of the phenazine unit (Fig. 4e). The Gibbs free energy associated with *OOH formation in this

scenario is −0.08 eV, a value markedly higher than that obtained during the reversible phenazine–dihydrophenazine conversion (−0.24 eV). This finding highlights the crucial role of phenazine–dihydrophenazine interconversion in reducing the energy barrier for $O_2$ reduction to facilitate $H_2O_2$ production.

Combining both experimental evidence and computational results, we have elucidated a comprehensive reaction mechanism for high-efficiency $H_2O_2$ production by TPE-PNZ. Initially, upon photoirradiation, the phenazine moiety in TPE-PNZ undergoes a redox process, wherein it captures two photogenerated electrons along with two protons, resulting in its conversion to dihydrophenazine. Following this reduction, $O_2$ is adsorbed onto the dihydrophenazine unit, where it engages in a sequential, single-electron transfer process, receiving two electrons and two protons from dihydrophenazine. This reaction leads to the direct synthesis of $H_2O_2$, concurrently regenerating the phenazine unit by oxidizing dihydrophenazine back to its original state, as illustrated in Fig. 5. This intricate interplay of redox reactions and electron–proton transfers points out a clear pathway for the efficient production of $H_2O_2$, highlighting the pivotal role of the phenazine moiety within the TPE-PNZ framework.

## Conclusions

In summary, our study unambiguously indicates that embedding the redox-active phenazine moiety within CMPs can markedly enhance the efficiency of photocatalytic $H_2O_2$ generation. This enhancement is primarily attributed to the phenazine units acting as critical sites for the reduction of $O_2$ and promoting effective charge separation within the polymer framework. More importantly, our study sheds light on the

fundamental principles guiding the molecular design of metal-free polymers for photocatalytic applications. This approach not only exemplifies the strategic incorporation of functional moieties to enhance photocatalytic efficiency but also offers a blueprint for the development of advanced materials aimed at harnessing solar energy for chemical synthesis.

## Data availability

The data that support the findings of this study are available from the corresponding author upon reasonable request.

## Author contributions

S. Feng, L. Wang and L. Tian synthesized the materials and performed the experiments. Y. Liu and H. Wang performed the DFT calculations. J. Hua and K. Hu wrote the manuscript. H. Xu modified the figures and the manuscript. H. Wang, H. Xu and J. Hua supervised and supervised the project. All authors discussed the results and contributed to the final manuscript.

## Conflicts of interest

There are no conflicts to declare.

## Acknowledgements

## Notes and references

1 J. Yue, L. Song, Y. Fan, Z. Pan, P. Yang, Y. Ma, Q. Xu and B. Tang, *Angew. Chem., Int. Ed.*, 2023, **62**, e202309624.

2 Y. Hou, P. Zhou, F. Liu, Y. Lu, H. Tan, Z. Li, M. Tong and J. Ni, *Angew. Chem., Int. Ed.*, 2024, **63**, e202318562.

3 Y. Luo, B. Zhang, C. Liu, D. Xia, X. Ou, Y. Cai, Y. Zhou, J. Jiang and B. Han, *Angew. Chem., Int. Ed.*, 2023, **62**, e202305355.

4 D. Chen, W. Chen, Y. Wu, L. Wang, X. Wu, H. Xu and L. Chen, *Angew. Chem., Int. Ed.*, 2023, **62**, e202217479.

5 T. Gao, C. Yang, Y. Zheng, Y. Shen, Q. Wang, L. Wang, R. Xu, M. Lv, M. Li, Z. Shi, L. Wang, X. Kong and L. Ye, *Appl. Catal., B*, 2024, **346**, 123761.

6 L. Wang, L. Liu, Y. Li, Y. Xu, W. Nie, Z. Cheng, Q. Zhou, L. Wang and Z. Fan, *Adv. Energy Mater.*, 2023, **14**, 2303346.

7 X. Xu, Y. Sui, W. Chen, W. Huang, X. Li, Y. Li, D. Liu, S. Gao, W. Wu, C. Pan, H. Zhong, H. Wen and M. Wen, *Appl. Catal., B*, 2024, **341**, 123271.

8 Z. Yong and T. Ma, *Angew. Chem., Int. Ed.*, 2023, **62**, e202308980.

9 J. B. Laursen and J. Nielsen, *Chem. Rev.*, 2004, **104**, 1663–1686.

10 N. A. Romero and D. A. Nicewicz, *Chem. Rev.*, 2016, **116**, 10075–10166.

11 X. Xu, R. Sa, W. Huang, Y. Sui, W. Chen, G. Zhou, X. Li, Y. Li and H. Zhong, *ACS Catal.*, 2022, **12**, 12954–12963.

12 H. Cheng, H. Lv, J. Cheng, L. Wang, X. Wu and H. Xu, *Adv. Mater.*, 2022, **34**, 2107480.

13 L. Chen, L. Wang, Y. Wan, Y. Zhang, Z. Qi, X. Wu and H. Xu, *Adv. Mater.*, 2020, **32**, e1904433.

14 Q. Zhi, W. P. Liu, R. Jiang, X. Zhan, Y. Jin, X. Chen, X. Yang, K. Wang, W. Cao, D. Qi and J. Jiang, *J. Am. Chem. Soc.*, 2022, **144**, 21328–21336.

15 J. M. Lee and A. I. Cooper, *Chem. Rev.*, 2020, **120**, 2171–2214.

16 J. Jeromenok and J. Weber, *Langmuir*, 2013, **29**, 12982–12989.

17 B. Ghanem, N. McKeown, P. Budd, J. Selbie and D. Fritsch, *Adv. Mater.*, 2008, **20**, 2766–2771.

18 J. Chang, Q. Li, J. Shi, M. Zhang, L. Zhang, S. Li, Y. Chen, S. Li and Y. Lan, *Angew. Chem., Int. Ed.*, 2023, **62**, e202218868.

19 J. Zhou, Y. Wang, Z. Cui, Y. Hu, X. Hao, Y. Wang and Z. Zou, *Appl. Catal., B*, 2020, **277**, 119228.

20 J. Wang, W. Shi, D. Liu, Z. Zhang, Y. Zhu and D. Wang, *Appl. Catal., B*, 2017, **202**, 289–297.

21 C. Wu, Z. Teng, C. Yang, F. Chen, H. Yang, L. Wang, H. Xu, B. Liu, G. Zheng and Q. Han, *Adv. Mater.*, 2022, **34**, 2110266.

22 L. Cao, C. Wang, H. Wang, X. Xu, X. Tao, H. Tan and G. Zhu, *Angew. Chem., Int. Ed.*, 2024, **63**, e2024020.

23 H. Yan, M. Shen, Y. Shen, X. Wang, W. Lin, J. Pan, J. He, Y. Ye, X. Yang, F. Zhu, J. Xu, J. He and G. Ouyang, *Proc. Natl. Acad. Sci. U.S.A.*, 2022, **119**, e2202913119.

24 Y. Guo, Y. Dong, B. Liu, B. Ni, C. Pan, J. Zhang, H. Zhao, G. Wang and Y. Zhu, *Adv. Funct. Mater.*, 2024, 2402920.

25 Y. Ye, J. Pan, Y. Shen, M. Shen, H. Yan, J. He, X. Yang, F. Zhu, J. Xu, J. He and G. Ouyang, *Proc. Natl. Acad. Sci. U.S.A.*, 2021, **118**, e2115666118.

26 X. Li, G. Zhang, N. Li, Q. Xu, H. Li, J. Lu and D. Chen, *Adv. Funct. Mater.*, 2024, 2316773.

27 X. Xia, J. Feng, Z. Zhong, X. Yang, N. Li, D. Chen, Y. Li, Q. Xu and J. Lu, *Adv. Funct. Mater.*, 2023, **34**, 2311987.

28 T. Yang, Y. Jin, Y. Wang, A. Kong, Y. Chen, Y. Zou, C. Liu, G. Wei and C. Yu, *Adv. Funct. Mater.*, 2023, **33**, 2300714.

29 Y. Yang, Q. Guo, Q. Li, L. Guo, H. Chu, L. Liao, X. Wang, Z. Li and W. Zhou, *Adv. Funct. Mater.*, 2024, 2400612.

30 Q. Zhang, J. Zhou, H. Zhang, C. Qi, Q. Zhou, R. Guo, H. Yang, T. Xing, M. Wang, M. Wu and W. Wu, *Adv. Funct. Mater.*, 2024, 2401579.

31 Z. Luo, X. Chen, Y. Hu, X. Chen, W. Lin, X. Wu and X. Wang, *Angew. Chem., Int. Ed.*, 2023, **62**, e202304875.

32 P. Gao, C. Wu, S. Wang, G. Zheng and Q. Han, *J. Colloid Interface Sci.*, 2023, **650**, 40–46.

33 R. Zhang, H. Zhao, C. Pan, J. Zhang, L. Jian, X. Sun, R. Ji, J. Li, Y. Dong and Y. Zhu, *New J. Chem.*, 2024, **48**, 3316–3324.

34 X. Xu, Y. Sui, W. Chen, G. Zhou, Y. Li, H. Zhong and H. Wen, *ACS Appl. Polym. Mater.*, 2023, **5**, 7571–7580.

35 C. Chu, D. Yao, Z. Chen, X. Liu, Q. Huang, Q. Li and S. Mao, *Small*, 2023, **19**, 2303796.

36  L. Li, Z. Cai, Q. Wu, W. Lo, N. Zhang, L. X. Chen and L. Yu, *J. Am. Chem. Soc.*, 2016, **138**, 7681–7686.

37  J. Xiong, X. Li, J. Huang, X. Gao, Z. Chen, J. Liu, H. Li, B. Kang, W. Yao and Y. Zhu, *Appl. Catal., B*, 2020, **266**, 118602.

38  H. Zhang, X. Chen, Z. Zhang, K. Yu, W. Zhu and Y. Zhu, *Appl. Catal., B*, 2021, **287**, 119957.

39  L. Yang, J. Yuan, G. Wang, Q. Cao, C. Zhang, M. Li, J. Shao, Y. Xu, H. Li and J. Lu, *Adv. Funct. Mater.*, 2023, **33**, 2300954.

40  B. Cai, H. Song, A. Brnovic, M. V. Pavliuk, L. Hammarström and H. Tian, *J. Am. Chem. Soc.*, 2023, **145**, 18687–18692.

41  C. Zhao, X. Wang, Y. Yin, W. Tian, G. Zeng, H. Li, S. Ye, L. Wu and J. Liu, *Angew. Chem., Int. Ed.*, 2023, **62**, e202218318.

42  C. Ye, J. Li, Z. Li, X. Li, X. Fan, L. Zhang, B. Chen, C. Tung and L. Wu, *ACS Catal.*, 2015, **5**, 6973–6979.

43  Y. Negishi, Y. Matsuura, R. Tomizawa, W. Kurashige, Y. Niihori, T. Takayama, A. Iwase and A. Kudo, *J. Phys. Chem. C*, 2015, **119**, 11224–11232.

44  Z. Wei, M. Liu, Z. Zhang, W. Yao, H. Tan and Y. Zhu, *Energy Environ. Sci.*, 2018, **11**, 2581–2589.

45  P. Li, F. Ge, Y. Yang, T. Wang, X. Zhang, K. Zhang and J. Shen, *Angew. Chem., Int. Ed.*, 2024, e202319885.

46  D. Chen, W. Chen, Y. Wu, L. Wang, X. Wu, H. Xu and L. Chen, *Angew. Chem., Int. Ed.*, 2023, **62**, 202217479.

47  D. Tan, R. Zhuang, R. Chen, M. Ban, W. Feng, F. Xu, X. Chen and Q. Wang, *Adv. Funct. Mater.*, 2024, **34**, 2311655.

48  X. Zeng, Y. Liu, X. Hu and X. Zhang, *Green Chem.*, 2021, **23**, 1466–1494.

49  Y. Kou, Y. Xu, Z. Guo and D. Jiang, *Angew. Chem., Int. Ed.*, 2011, **50**, 8753–8757.

50  X. Gao, Y. Chen, C. Gu, J. Wen, X. Peng, J. Liu, Z. Zhang, Q. Zhang, Z. Liu and C. Wang, *J. Mater. Chem. A*, 2020, **8**, 19283–19289.

51  Z. Wei, S. Zhao, W. Li, X. Zhao, C. Chen, D. L. Phillips, Y. Zhu and W. Choi, *ACS Catal.*, 2022, **12**, 11436–11443.

52  D. Lee, M. Park, N. Kim, M. Gu, H. Kim and B. Kim, *J. Catal.*, 2022, **411**, 235–244.

53  L. Zhang, Y. Huang, H. Yan, Y. Cheng, Y. X. Ye, F. Zhu and G. Ouyang, *Adv. Mater.*, 2024, 2401162.

54  Q. Ruan, X. Xi, B. Yan, L. Kong, C. Jiang, J. Tang and Z. Sun, *Chem*, 2023, **9**, 1850–1864.